# Material Sensing Using RAIN RFID Tags With Auto-Tuning Capabilities

Rahul Bhattacharyya<sup>®</sup>, *Senior Member, IEEE*, Fatima Villa Gonzalez<sup>®</sup>, *Member, IEEE*, and Pavel Nikitin<sup>®</sup>, *Fellow, IEEE* 

Abstract-In this paper, we demonstrate how the poweron-tag-forward (POTF) and reverse (POTR) resonance frequencies can be estimated simply by measuring changes in the autotune (AT) code of RAIN RFID chips capable of making capacitance adjustments for enhanced antenna impedance matching. We show how this approach allows us to reliably estimate these characteristic frequencies — and, by extension, the dielectric and magnetic properties — of objects using a simple reading of the AT state values in the chip memory. Therefore, we eliminate the need for full POTF and/or POTR curve measurement and the need for read distance estimation and environmental calibration. The proposed method shows repeatability using 6 diverse RAIN RFID tags with T-matched antenna designs and self-tuning ICs, deployed on 7 dielectrics and 1 magnetic material. Current limitations and future research directions are also discussed.

Index Terms—Auto-tuning ICs, material sensing, RAIN RFID tags, power-on-tag-forward, power-on-tag-reverse.

#### I. INTRODUCTION

Reduction in tag costs has contributed to an increase in the granularity of RFID tag deployment [1]. Recently, major retailers, such as Walmart, have mandated item-level tagging for more products [2]. RFID tags on product packaging could be used to sense the underlying material and improve the quality control of material recovery after disposal. With only 9% plastics recycled in the US [3], there is a dire need to improve the efficiency of material recovery in the circular economy.

The T-matched dipole antenna, where a dipole antenna is coupled to a loop [4], is one of the common antenna structures used in RAIN RFID tags because it provides a good impedance match on various materials. RAIN RFID tags are characterized by threshold sensitivity and backscatter, called threshold power-on-tag-forward (POTF) and power-on-tag-reverse (POTR) as introduced by Voyantic [5]. As explained by Nikitin et al. [6], T-matched tags have three resonant frequencies (c.f. Fig. 1): two are minima of POTF ( $f_a$  and  $f_b$ )

Received 14 April 2025; revised 21 May 2025; accepted 26 May 2025. Date of publication 29 May 2025; date of current version 16 June 2025. (Corresponding author: Fátima Villa González.)

Rahul Bhattacharyya and Fatima Villa Gonzalez are with the Auto ID Labs, Massachusetts Institute of Technology, Cambridge, MA 02139 USA (e-mail: rahul\_b@mit.edu; fatimavi@mit.edu).

Pavel Nikitin is with Impinj Inc., Seattle, WA 98109 USA (e-mail: nikitin@ieee.org).

Digital Object Identifier 10.1109/JRFID.2025.3575043

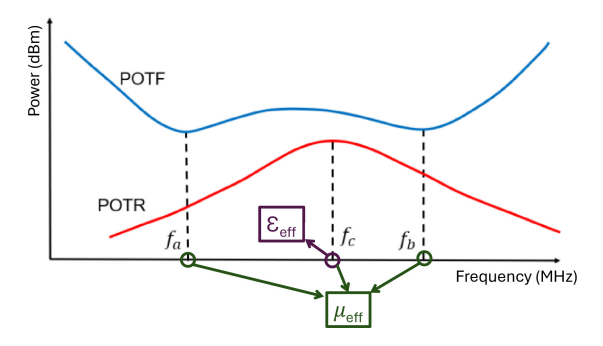


Fig. 1. General POTR and POTF curves of a T-matched RAIN RFID tag with resonances marked. Shifts in these can be related to  $\epsilon_{eff}$  and  $\mu_{eff}$ .

and the third is the maximum of POTR  $(f_c)$ . These are related to the natural resonant frequency of the dipole antenna,  $f_1$  and of the loop portion of the tag,  $f_2$  [6].

Nikitin et al. subsequently demonstrated how shifts in the POTR resonance frequency,  $f_c$ , are used to determine effective dielectric permittivity ( $\epsilon_{eff}$ ) of tagged materials [7] and shifts in  $f_a$ ,  $f_b$  and  $f_c$  can be used to estimate effective magnetic permeability ( $\mu_{eff}$ ) [8] (see Table I). However, identifying resonance frequencies involves the use of a precision tag power measurement reader [5] as well as environmental calibration.

There also exist several commercial chips (ICs) which have a self or auto-tuning feature, where IC impedance automatically adjusts to antenna reactance by applying an appropriate capacitance. The capacitance value is stored as a digital code in the user accessible tag memory. Recent generations of Impinj ICs apply a capacitance adjustment of 200 fF in 4 steps (known as the *Auto-Tune (AT)* code) [9]. There exist other chips with similar features, such as recent generations of NXP ICs, which have capacitance adjustment of 160 fF in 2 steps [10] and the Magnus IC from Axzon, which has a larger adjustment range of 1 pF in 511 steps [11]. Another IC, the AS2313 IC by Asygn has a 10-bit ADC and can measure an external capacitance in the range between 1 and 7 pF [12].

As listed in Table I, sensors using the Magnus IC have been used to detect fill-level [13], dielectric property estimation and material identification [14], [15], [16], [17], [18], potentiometric sensing [19] and AC current detection [20] based on capacitive code value changes. The AS2313 IC has also been used for strain [21] and humidity sensing [22]. In addition, Zannas et al. used Impinj IC AT code changes with a custom antenna for temperature sensing [23]. However, to the best of

Ref.	Application	IC	Monitored parameter(s)	How are they monitored	Physical meaning	Notes
[23]	Temperature sensing	Impinj Monza R6	$f_a$	Capacitive code value (AT)	$f_a$ is a complicated non-linear function of $\epsilon$	Low resolution and tedious antenna tuning
[14]–[16], [19]	Potentiometric and material sensing	Magnus	$f_a$ or $f_b$	Capacitive code value		Simple method but
[17], [18]	Material sensing	Series ICs	$f_a$ or $f_b$	(sensor code)	$f_a$ and $f_b$ are complicated non-linear functions of $\epsilon$ and $V$	sometimes requires
[20]	AC current sensing		$f_a$			tuning circuit or IDC for $V$ to $C$ conversion <sup>1</sup>
[22]	Humidity and strain sensing	AS2313 IC	$f_a$ or $f_b$	Capacitive code value (temperature and strain codes)		
[7]	Dielectric sensing	Impinj M730 Impinj Monza 4, 5, R6	$f_c$	Shape of measured POTR curve	$f_c \propto f_1 \propto \frac{1}{\sqrt{\epsilon}}$	Requires wideband measurements with expensive equipment
[8]	Magnetic sensing	Impinj M730 Impinj Monza R6	$f_a, f_b$ $f_c$	Shapes of measured POTF and POTR curves, then $f_1, f_2, k$ are calculated	$f_2 \propto rac{1}{\sqrt{\mu}}$	Same as above + AT needs to be disabled
This	Dielectric sensing	Impinj M750		$f_1$ found from positive transitions of AT code, then $f_c$ is computed	$f_c \propto \frac{1}{\sqrt{\epsilon}}$	Requires wideband measurements of the
work	Magnetic sensing	Impinj M730 Impinj Monza R6	$f_a, f_b$ $f_1$	Same as above + $f_a$ and $f_b$ found from negative transitions of AT code, then $f_2$ is computed	$f_2 \propto rac{1}{\sqrt{\mu}}$	AT code, but not of the POTF, POTR + AT does not need to be disabled

TABLE I
REPORTED SENSING APPROACHES USING AUTO-TUNING ICS

our knowledge, Zannas' work is the only prior art exploiting the capacitive code of Impinj chips. The Magnus IC and the AS2313 IC, while being more versatile and even marketed for sensing purposes, are also more expensive due to the increased complexity of the onboard electronics [24].

All published works using auto-tuning ICs, whether from Impinj, Axzon or Asygn, focus on monitoring the associated capacitive code value at POTF resonance frequencies,  $f_{a/b}$  (see Table I). However, as seen in [6], POTF resonances are complicated functions of dipole, loop, coupling and chip impedance characteristics. Reliably determining these resonances therefore requires disabling the auto-tune adjustment feature on the chips prior to re-engaging it for sensing purposes. These procedures are cumbersome and add latency to the sensing process. Besides, relating the digital output of the IC to variations in the sensing stimuli at  $f_{a/b}$ , often involves solving complex optimization problems with advanced mathematical modeling and computational resources [19].

In this paper, we demonstrate how the shape of the AT code variation with frequency can be used to reliably determine or derive  $f_a$ ,  $f_b$  and  $f_c$  without the need for generating the POTF and POTR curves. This obviates the need to use precision power measurement equipment and reduces reliance on environmental calibration and reader-tag read distance. We also demonstrate how AT code markers may therefore be used for both  $\epsilon_{eff}$  and  $\mu_{eff}$  estimation of materials. Our approach can be viewed as a form of near-field sensing since AT code is not affected by the far-field reader-tag channel characteristics and is affected only by interaction of the tag antenna with a dielectric or magnetic object in its near field.

The rest of the paper is organized as follows. Section II discusses our hypothesis of how AT code markers can be used to detect the resonance frequencies in the POTR and POTF curves. Section III presents the tags used, materials tested, hardware setup and the data capture procedure. Sections IV and V discuss dielectric and magnetic sensing

TABLE II CHARACTERISTIC ANGULAR FREQUENCIES ( $\omega=2\pi f$ ) of RFID Tags With T-Matched Antenna Structure. Also Shown Are the Dependence on Material Properties ( $\epsilon$  and  $\mu$ )

$\omega$	Definition	Formula	Material dependence $(\mu, \epsilon)$	
$w_1$	Natural res. freq. of dipole	$w_1 = \frac{1}{\sqrt{L_1 C_1}}$	Depends on $\mu$ and $\epsilon$ $(L_1 \propto \mu, C_1 \propto \epsilon)$	
$w_2$	Natural res. freq. of loop	$w_2 = \frac{1}{\sqrt{L_2 C_p}}$	Depends on $\mu$ only $(L_2 \propto \mu)$	
$w_a$	Lower POTF res. freq.	$w_{a,b}^2 = \frac{w_1^2 + w_2^2}{2(1 - k^2)} \pm$	Depend on $\mu$ and $\epsilon$	
$w_b$	Higher POTF res. freq.	$\pm \frac{\sqrt{(w_1^2 - w_2^2) + 4k^2 w_1^2 w_2^2}}{2(1 - k^2)}$	(see $w_1$ , $w_2$ and $k$ )	
$w_c$	POTR res. freq.	$w_c^2 = \frac{w_1^2}{1 - k^2}$	Depend on $\mu$ and $\epsilon$ (see $w_1$ )	
k	Coupling coefficient	$k = \sqrt{1 - \frac{\omega_2^2}{\omega_a^2 + \omega_b^2 - \omega_c^2}}$	Depends on $\mu$ only $(L_1 \propto \mu, L_2 \propto \mu)$	

results, respectively, using AT code markers in both idealized and real-world environments. Finally, Section VII presents the main conclusions and future research directions.

# II. HYPOTHESIS: AT CODE MARKERS FOR RESONANCE FREQUENCY DETECTION

Nikitin et al. presented closed form circuit equations of the characteristic frequencies of a T-matched antenna structure [6]. These are summarized in Table II.

Nikitin et al. also presented the equivalent circuit parameters of a generic T-matched tag with a specific geometry [25]. We therefore use the circuit model in [6] and parameters from [25] to illustrate our hypothesis. Computations are based on the Impinj Monza M700 series of IC, with 1.04 pF base  $C_p$  and  $\pm 40$  fF,  $\pm 100$  fF capacitance adjustments with AT codes from 0 to 4 [26]. Fig. 2 illustrates the computed tag characteristics and how they relate to AT code states when the tag is in air:

• Fig. 2(a) presents the computed POTF and POTR curves using Eq. (5) in [6]. POTF is obtained using Eq.(2) in [6].

 $<sup>^{1}</sup>V$  stands for voltage, C for capacitance and IDC for Interdigitated capacitor.

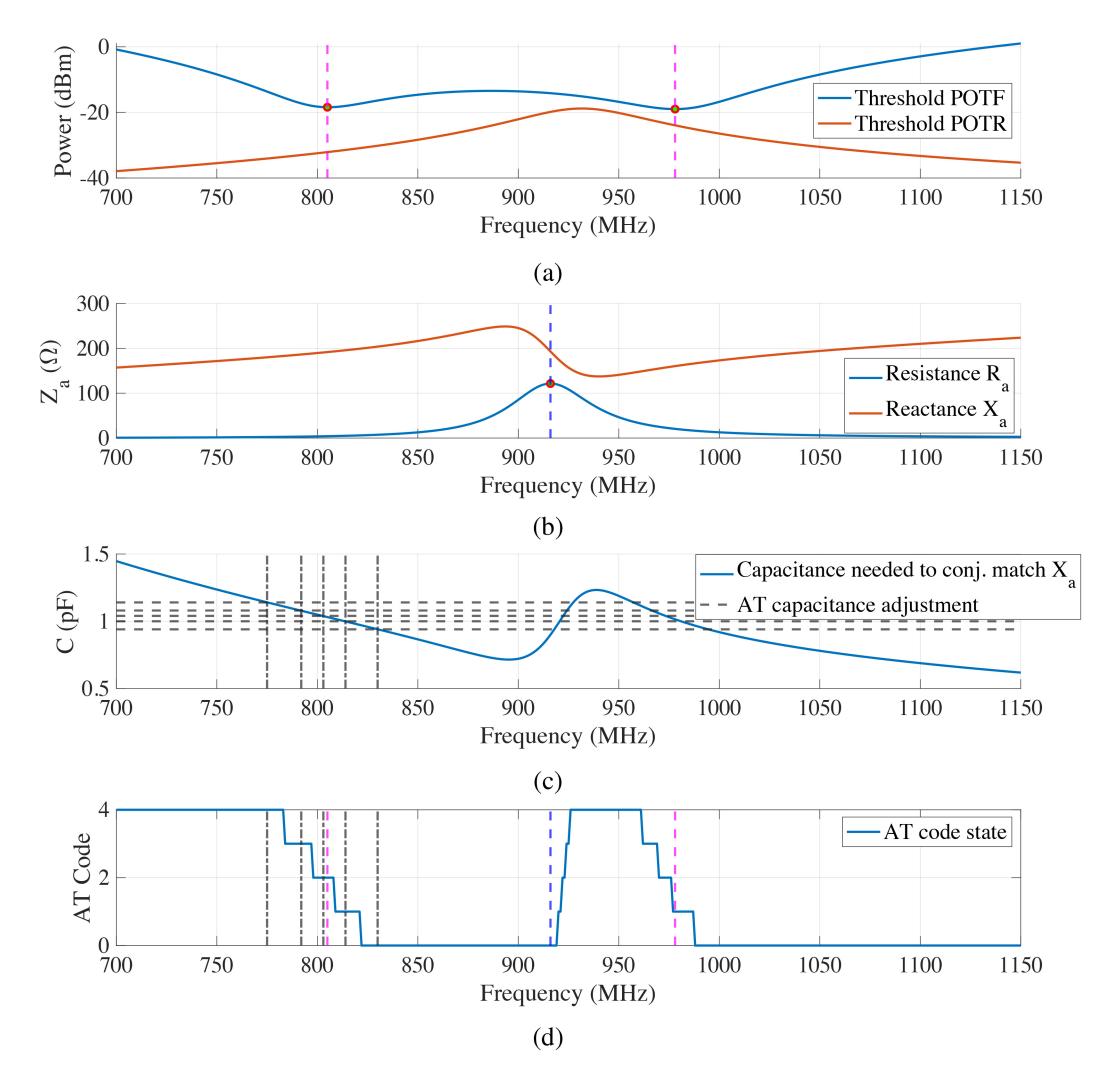


Fig. 2. Computed circuit parameters of a generic T-matched tag in [25]: (a) POTF and POTR curves (b) Antenna impedance  $Z_a$  (c) Chip capacitance needed to conjugate match antenna reactance (d) AT code state.

We assume the antenna gain, G = -2 dBi, constant across the band, polarization mismatch factor, p = 1, and a modulating resistance of 50  $\Omega$ .

- Fig. 2(b) presents the antenna resistance and reactance using [6, Eq.(7)].
- Fig. 2(c) presents the chip impedance required to conjugate match the antenna reactance. Also shown in the figure are 5 capacitance auto-tune adjustments that can be applied by the chip (AT code 0 through 4).
- Fig. 2(d) illustrates the change in AT state as a function of frequency. When the required capacitance for matching is either too high or too low, the chip applies the maximum or minimum adjustment capacitance corresponding to AT = 4 and AT = 0 respectively. When the required capacitance is within the adjustment band, however, an appropriate AT code is chosen.

From Fig. 2, we notice that reactance values that fall within the capacitive tuning band exhibit noticeable changes about the resonance frequencies  $\omega_a$  and  $\omega_b$  and  $\omega_1$ . Specifically,  $\omega_a$ and  $\omega_b$  align with the middle of a decrease of AT from 4 to 0, while  $\omega_1$  aligns with an increase of AT from 0 to 4. These three values can therefore be estimated by the AT shape features, i.e., the two magenta and blue marker lines in Fig. 2(d).

Now that we have found frequencies  $\omega_a$  and  $\omega_b$  and  $\omega_1$ (from AT code transitions), the remaining two resonance frequencies listed in Table II, can be derived as follows:

$$\omega_c = \sqrt{\omega_a^2 + \omega_b^2 - \frac{\omega_a^2 \omega_b^2}{\omega_1^2}} \tag{1}$$

$$\omega_c = \sqrt{\omega_a^2 + \omega_b^2 - \frac{\omega_a^2 \omega_b^2}{\omega_1^2}}$$

$$\omega_2 = \frac{\omega_a \omega_b}{\sqrt{\omega_a^2 + \omega_b^2 - \frac{\omega_a^2 \omega_b^2}{\omega_1^2}}}.$$
(2)

In the subsequent sections, we will examine if this hypothesis can be generalized using 6 different RFID tags with different antenna designs and ICs with AT capabilities. The only constraint is that all tags need to have a T-matched antenna design, which is the prevailing design of antennas in RFID inlays. We will also determine the effect of attaching the tag to materials with different  $\epsilon$  and  $\mu$  and verify if the hypothesis can be used for  $\epsilon_{eff}$  and  $\mu_{eff}$  estimation and hence material detection.

TABLE III
T-MATCHED RAIN RFID TAGS USED IN THIS STUDY

Tag	Model	Size (mm)	1 17		Image	
1	Beontag A701	42 x 16				
2	Beontag A701 (1 meander cut)	38 x 16	Impinj Monza M750	Monza	0.925	
3	Beontag A701 (2 meanders cut)	34 x 16				
4	Arizon AZ-MR71	42 x 16	Impinj Monza M730	0.925	ESIZ - 10 165 OKOLSP OVOKAD	
5	Arizon AR-61F	40 x 15	Impinj Monza	1.230		
6	Beontag H61	50 x 30	R6	I		

#### III. EXPERIMENTAL SETUP

The RAIN RFID tags and materials used, the reader hardware, environmental setup, and data capture procedure are discussed in this section.

# A. RAIN RFID Tags

Table III shows the tags used in the study. The tags have different antenna shapes and utilize at least 3 different chips with AT adjustment capabilities (AT code 0 through 4 and  $\pm$  100 fF  $C_p$  adjustments). All tags have a T-match structure, which is found across a plurality of ARC certified tags [27].

Note that Tags 2 and 3 are modified antenna versions of Tag 1. Cutting meander sections reduces the length of the dipole, therefore changes dipole response and allows one to create a large number of differently tuned antennas.

#### B. Materials Tested

We use the reference material kit provided by Voyantic for  $\epsilon_{eff}$  estimation [28]. The materials and their dielectric properties are summarized in Table IV. The materials are available in 130 x 130 mm sheets, 4 mm thick. For magnetic sensing, we used 130 x 65 mm magneto-dielectric sheets of a flexible absorbent material (FAM) from Delevan, which are 0.12 mm thick [29]. All materials are shown in Fig. 3.

#### C. Reader Hardware and Test Setup

We use the Voyantic Tagformance Broadband kit [5], which is capable of testing tags in the 600-1300 MHz band, as the reader for all our experiments. For the dielectric sensing, we conduct two sets of tests:

• We conduct 3 experiments using Tags 1-3 in an anechoic chamber on PTFE, PVC, Rubber, POM and PVC. This is

TABLE IV
MATERIAL PROPERTIES IN THE VOYANTIC KIT

Material	$\epsilon_r$	$tan(\delta)$
PTFE	2.05	0.0002
Cardboard (CB)	2.57	0.0717
POM	2.96	0.0450
PVC	3.00	0.0079
FR-4	4.87	0.0141
Rubber	6.73	0.0247
Glass	7.11	0.0098



Fig. 3. Materials used for  $\epsilon_{eff}$  and  $\mu_{eff}$  sensing.

- meant to represent idealized performance (c.f. Fig. 4 (a)-(b)). The tag under test (TUT) is placed on the material under test (MUT) with the antenna side facing down and a constant even pressure is applied using the foam spacing to press the tag firmly against the surface, ensuring it lies flat and eliminating any air gaps.
- We conduct 4 experiments using Tags 1 and 4-6 on all 7 materials in an open warehouse environment (c.f. Fig. 4 (c)). We eliminate clutter around the setup but do not take any steps to mitigate environmental reflections. Clear adhesive tape is used to apply the TUT to the MUT. The MUT is mounted vertically with the antenna facing to a side. This scenario is meant represent real world conditions. As an example, Fig. 5 shows some of the utilized tags attached to FR-4 and FAM sheets.

For the magnetic sensing, we conduct experiments using Tags 5 and 6 by measuring their performance on the FAM material. The tests are conducted in an idealized environment and the TUT is placed on the FAM sheet with the antenna side facing down. A constant even pressure is applied using the foam spacing to eliminate any air gap.

It is important to note that polarization matching between the reader and tag antennas is not strictly necessary for the proposed approach. Changing the polarization of the reader antenna will affect the propagation loss between reader and tag antennas and hence the power levels of the measured POTF and POTR curves, but it will not alter their shape. Therefore, the behavior of the AT code transitions will remain consistent regardless of polarization alignment.

# D. Data Capture Procedure

The dielectric sensing tests in the idealized environment and the magnetic sensing tests are conducted using the *Read 640K FM0* mode in Voyantic, which represents the highest

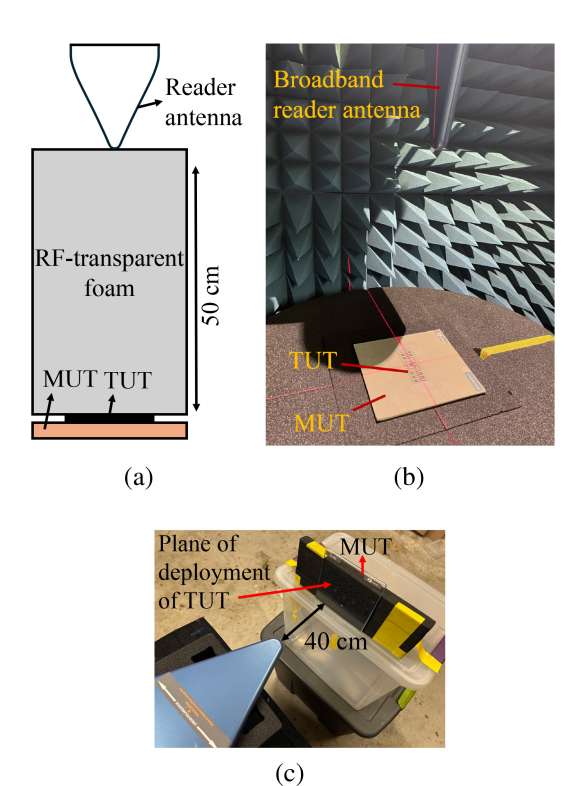


Fig. 4. Experimental setup: (a) diagram of ideal test setup, (b) laboratory test setup with foam removed for visibility, and (c) real world setup.



Fig. 5. Examples of tags attached to material sheets using clear tape: Tag 4 on FR-4 and Tag 1 on FAM.

read speed mode available in the Gen2 protocol. This mode enables data to be read from the tag memory at the maximum achievable speed, enhancing the overall efficiency and speed of the testing process. The dielectric sensing tests conducted in the real world scenario (Fig. 4(c)), are done at a different mode *Read 40K FM0*, just as a point of comparison. For each TUT on each MUT, the testing procedure occurs as follows:

- First, the threshold sweep is conducted with AT enabled.
   The POTR curve and AT code over the 600-1300 MHz band is recorded.
- Second, the AT feature is disabled and the threshold sweep is run again so that  $\omega_a$  and  $\omega_b$  can be extracted from the POTF curve as the ground truth. This is necessary because from Eq. (4) in [6], we see that both are dependent on the chip impedance, which can be masked if AT is enabled.

#### IV. DIELECTRIC SENSING USING AT CODE MARKERS

Fig. 6 demonstrates the working of our hypothesis in an experimental setting. Here the performance of the A701 tag (Tag 1 in Table III) is examined in an idealized environment on air, PVC and rubber as a backing material:

- The top row shows the change in AT code vs. frequency.
   The markers corresponding to the estimated values of fa and fb are marked with magenta vertical lines and f1 with a red vertical line. In order to standardize the positioning of this line, we assume it goes through the midpoint of the positive AT slope increase.
- The middle row shows the POTF curves with the true values of  $f_a$  and  $f_b$ . We observe that the AT markers align very well with these.
- The bottom row shows the POTR curve with the true peak value marked. Also shown is the estimated value corresponding to Eq. (1) (marked with a blue vertical line). In general, the true and estimated values align very well but there is a small discrepancy that may be caused by minor fluctuation of  $f_1$  due to small positional uncertainties of the marker line, environmental and material influences.

Table V highlights the estimated values of  $f_a$ ,  $f_b$  and  $f_1$  using the AT marker method for all the dielectric tests conducted in Section III-C. We use these to compute the estimated value of  $f_c$  using Eq. (1). Finally, this is compared to the true value of  $f_c$  extracted from the POTR curve. Table VI summarizes the discrepancy between the true and estimated value of  $f_c$  for each TUT and MUT for the results in Table V. The results are separated by experiments conducted in real vs. idealized settings. While it is expected that idealized tests perform better, real world performance degradation is not that significant. This indicates that the approach works even in the presence of complicating factors such as environmental reflections and when the tag is covered with adhesive tape — at least in situations where the tag and reader are close (40 cm) to one another.

Finally, the dielectric permittivity of the MUT is estimated using both the true and estimated values of  $f_c$  [7]:

$$\epsilon_{eff} = \frac{1}{(1 - \Delta_1)^2}, \text{ where } \Delta_1 = \frac{f_c^{air} - f_c^{MUT}}{f_c^{air}},$$
 (3)

and

$$\epsilon_{eff} = 1 + \frac{\epsilon_r - 1}{2} \frac{K2}{K1} \tag{4}$$

where K1 and K2 depend on the size and  $\epsilon_r$  of the dielectric material and geometry of the tag antenna [30]. However, since most T-matched UHF RFID tags utilize flat, centerfed meandered dipole antennas, K1 and K2 are not strongly dependent on antenna geometry for common UHF RFID tags [7]. Variations in dielectric slab thickness are expected to influence K1 and K2, and thus the standard error of the estimated  $\epsilon_{eff}$  for a given material. To mitigate this effect, we have used the well-characterized materials in the Voyantic testing kit, with uniform area and thickness.

Fig. 7 shows the relationship between  $\epsilon_{eff}$  and the relative permittivity  $\epsilon_r$  of the dielectric slab in both idealized and realworld testing environments. A consistent linear relationship

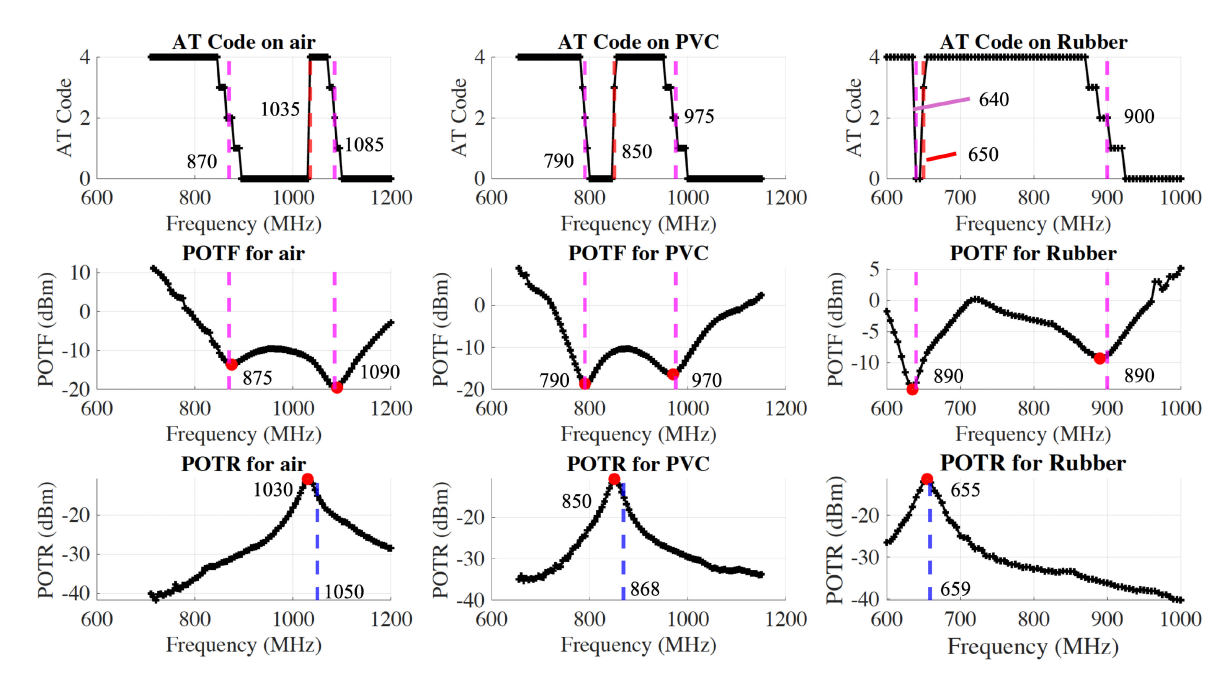


Fig. 6. Hypothesis tested with A701 tag on 3 dielectrics in an idealized environment.

TABLE V ESTIMATED VALUES OF  $f_a, f_b$  and  $f_1$  Using AT Marker Method, Computed Value of  $f_c$  and True Value of  $f_c$  for Different TUTs and MUTS

		Materials							
		Air	CB	PTFE	PVC	POM	FR4	RUBBER	GLASS
	$f_1$	1035	-	910	850	825	795	650	-
Tag 1	$f_a$	870	-	825	790	780	750	640	-
(Ideal setup)	$f_b$	1085	-	1010	975	960	945	900	-
(Ideal Setup)	$f_c$ (computed)	1050	-	929	868	840	813	659	-
	$f_{oldsymbol{c}}( ext{actual})$	1030	-	910	850	825	795	655	-
	$f_1$	1130	-	985	920	920	850	705	-
	$f_a$	885	-	850	825	825	785	680	-
Tag 2	$f_b$	1160	-	1055	1010	1005	970	910	-
	$f_c$ (computed)	1142	-	1003	938	937	869	721	-
	$f_c$ (actual)	1125	-	985	920	915	850	705	-
	$f_1$	1245	-	1085	1015	1010	930	760	-
	$f_a$	890	-	870	850	850	820	720	-
Tag 3	$f_b$	1260	-	1130	1070	1060	1010	925	-
	$f_c$ (computed)	1252	-	1101	1032	1025	948	779	-
	$f_c$ (actual)	1235	-	1080	1010	1005	925	765	-
	$f_1$	1035	940	910	860	845	790	695	695
Tag1	$oldsymbol{f_a}$	880	845	830	800	790	755	675	670
(Real-world setup)	$f_b$	1095	1025	1015	990	985	960	945	925
(Kear-world Setup)	$f_c$ (computed)	1052	957	928	879	864	806	712	714
	$f_c$ (actual)	1035	935	910	860	845	790	700	695
	$f_1$	1065	960	940	880	870	815	785	730
	$f_a$	890	855	850	820	815	780	755	710
Tag 4	$f_b$	1090	995	1000	970	960	940	945	915
	$f_c$ (computed)	1073	967	951	892	882	826	798	741
	$f_c$ (actual)	1055	955	935	880	865	815	785	730
	$f_1$	1180	1065	1035	965	955	895	790	780
	$f_{a}$	895	870	865	840	835	810	740	730
Tag 5	$f_b$	1205	1095	1090	1045	1035	1000	965	945
	$f_c$ (computed)	1191	1075	1052	985	974	915	813	802
	$f_c$ (actual)	1170	1045	1025	960	950	890	785	770
	$f_1$	985	895	875	825	820	765	700	680
	$f_a$	815	790	780	755	755	725	670	655
Tag 6	$f_b$	1015	940	935	905	905	880	865	855
	$f_c$ (computed)	995	905	888	839	834	777	715	694
	$f_c$ (actual)	975	880	865	815	815	760	695	680

All frequencies are in MHz.

is observed for both the true and computed  $f_c$  values. The estimated  $\epsilon_{eff}$  show larger standard errors for higher values of  $\epsilon_r$  (e.g.,  $\epsilon_r = 6.73$  and 7.11), which is consistent with theoretical

expectations. As indicated by Eq. (4), higher  $\epsilon_r$  increases the influence of the K2/K1 term, amplifying sensitivity to parameter variations and resulting in greater estimation uncertainty.

TABLE VI DISCREPANCY BETWEEN TRUE AND ESTIMATED VALUES OF  $f_{\it c}$  in Real and Idealized Environments

Test	Frequency difference in MHz					
environment	Max.	Min.	Mean.	Std.		
Idealized	23.00	4.00	17.83	4.22		
Real-world	32.00	11.00	19.56	5.63		

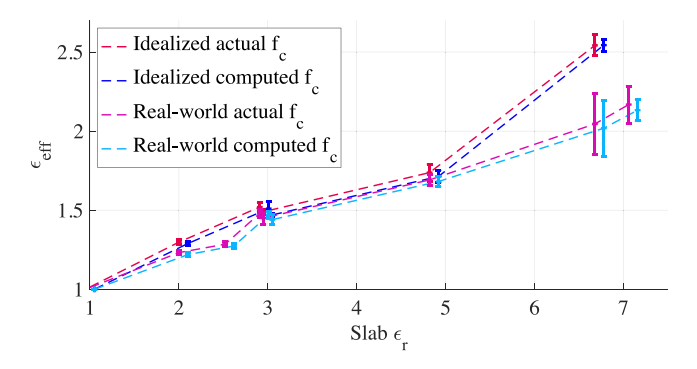


Fig. 7. Relationship between  $\epsilon_{\it eff}$  and slab  $\epsilon_{\it r}$  using computed and actual  $f_{\it C}$  in idealized and real-world environments.

There is good agreement between the real world and idealized tests for materials with lower  $\epsilon_r$ . For materials with higher  $\epsilon_r$ , there is more of a difference, which can be explained as follows: the rubber sheet is somewhat flexible and it tends to sag slightly especially when mounted vertically (c.f. Fig. 4(c)). This introduces a slight curvature which could delaminate the tag that is attached to the sheet using tape, thus introducing a small air gap. The glass tends to pick up adhesive residue from the tag or tape that is used to attach the tag to the surface. This residue was cleaned between successive tests using acetone. While we did our best to wait a sufficiently long amount of time between successive tag tests, it is possible that remnant acetone affected the attachment adhesive of the next TUT manifesting as a small air gap here as well. The introduction of these micro air gaps could explain why the mean values of  $\epsilon_r$  were consistently lower than those observed in the idealized tests. These effects and trends are consistent with prior observations (Fig. 8 in [7]) and support the conclusion that AT code transitions can be used effectively for dielectric sensing, even in the presence of real-world variability.

# V. MAGNETIC SENSING USING AT CODE MARKERS

We examine the applicability of our hypothesis to detect magneto-dielectric materials, specifically the FAM ferrite sheet in Fig. 3. Note that the FAM sheet has both  $\mu_r$  and  $\epsilon_r$  different from air. Both parameters have not been characterized for this material as reported by [8]. Furthermore, apart from  $f_a$ ,  $f_b$  and  $f_c$ , the coupling coefficient (k in Table II) will also be influenced by the magnetic material.

We therefore select Tag 5 to first validate our hypothesis. As seen in Table V, Tag 5 is the unmodified tag with the highest POTR peak frequency in air that we had available for testing and should therefore be able to accommodate the largest downshift in AT marker movement while still staying within the 600-1300 MHz band.

TABLE VII COMPARISON OF ESTIMATED  $\mu_{eff}$  OF THE FAM USING POTF AND POTR CURVES [8] AND AT CODE MARKERS

Tag	Frequency (MHz)	Mat	erial	Estimated
Tag	Frequency (WIIIz)	Air	FAM	$\mu_{eff}$
	$f_a$	885	778	
	$f_b$	1200	883	
5	$f_1$	1180	828	
	$f_2$ (from POTF/POTR)	946	861	1.20
	$f_2$ (from AT)	893	818	1.19
	$f_a$	810	725	
	$f_b$	1010	820	
6	$f_1$	988	773	
	$f_2$ (from POTF/POTR)	849	768	1.22
	$f_2$ (from AT)	829	757	1.20

Fig. 8 shows the performance of Tag 5 in the following situations:

- The first column shows the AT markers, POTF and POTR curves for air. The  $f_a$  and  $f_b$  marker positions, real and computed values of  $f_c$  align well with the ground truth.
- The second column shows the performance for the tag placed on FAM material. We notice a significant downshift in all resonance frequencies. Furthermore, the AT markers, while following the same shape, do not necessarily transit through all 4 AT code states. Nevertheless, there continues to be good agreement between the real and AT predicted resonance frequency values.
- The third column shows the performance of the tag sandwiched between the FAM and FR4 material. Unfortunately, it appears that both AT step markers corresponding to  $f_a$  and  $f_1$  have shifted below the 600 MHz lower bound of the Voyantic system and that the chip capacitance required to match the antenna reactance is too high.

In order to examine the repeatability of the approach, we also test Tag 6 (very different antenna shape and different chip as seen in Table III) in air and on the FAM material. The  $f_2$  values computed from the AT code markers and from  $f_a$ ,  $f_b$  and  $f_c$  in the POTF and POTR curves (as done in [8]) are presented and compared in Table VII. We estimate the effective magnetic permeability  $\mu_{eff}$  in both cases using [8]:

$$\mu_{eff} = \frac{1}{(1 - \Delta_2)^2}, \text{ where } \Delta_2 = \frac{f_2^{air} - f_2^{MUT}}{f_2^{air}}.$$
 (5)

From Table VII we see that the  $\mu_{eff}$  values between the 2 tags computed using both methods align well, indicating the potential of the proposed AT-based approach for sensing magneto-dielectric materials as well.

# VI. CURRENT LIMITATIONS

It is important to acknowledge the limitations associated with this work that are related to the capacitance matching capabilities of the Impinj ICs used in this paper.

Fig. 9 presents the results of two counter examples that we were able to find in our testing. In both tests, the positive AT step marker from 0-4 (corresponding to  $f_1$ ) that should be present to the left of the POTR peak is not visible:

• The 1<sup>st</sup> column of Fig. 9 are for the Avery Dennison Dogbone tag with the Monza R6 chip [31] in free space.

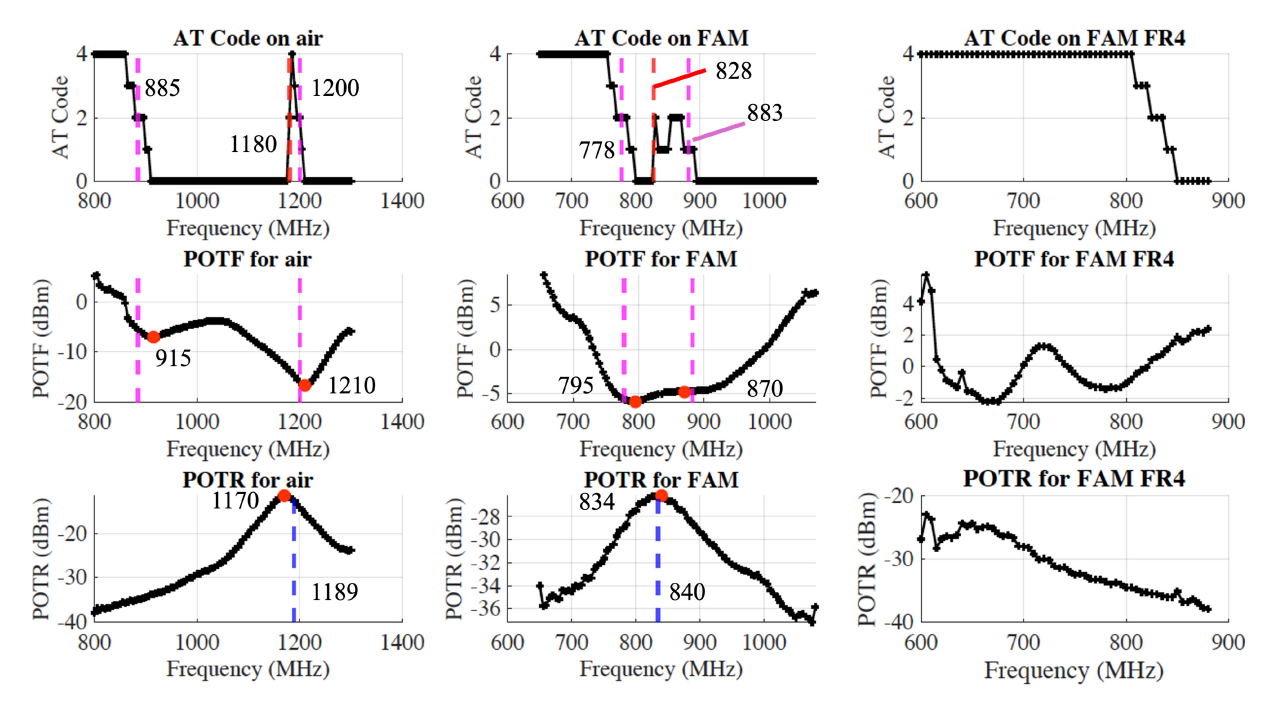


Fig. 8. Use of AT markers for resonance frequency estimation on magnetic materials.

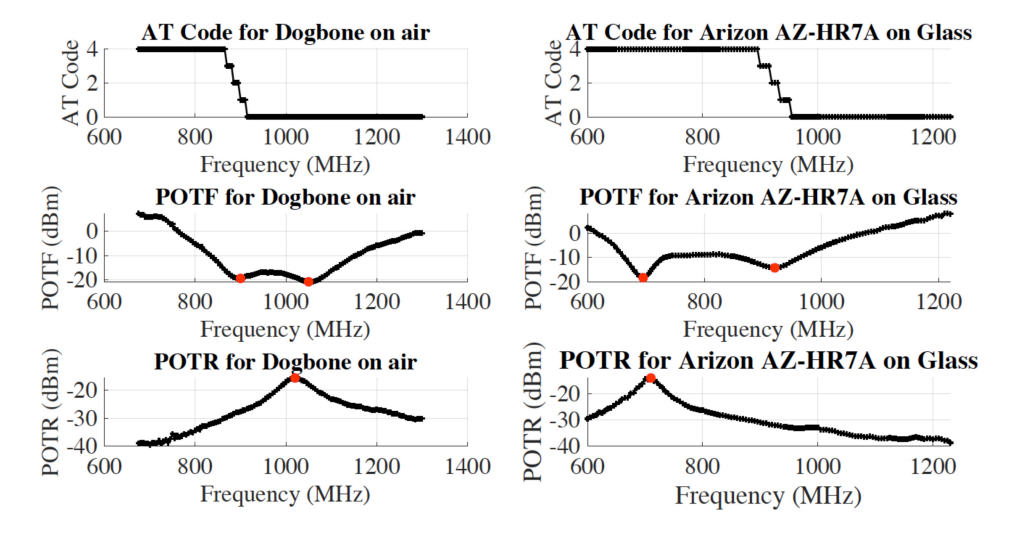


Fig. 9. Counterexamples illustrating the limitations of our hypothesis.

We surmise that the antenna reactance at  $f_1$  is too high so the required matching chip capacitance is too low. This is why the AT code is consistently at the lower bound of 0 in this region.

• The  $2^{nd}$  column of Fig. 9 shows the results of testing the Arizon AZ-HR7A with the M730 chip [32] on glass substrate. Here we theorize that the antenna reactance at  $f_1$  is too low so the chip capacitance required is too high and this is indicated by the AT code assuming the upper bound of 4 in this region.

We also noticed that not all tags in Table III generated the AT markers when deployed on the FAM material. The POTR peak of tag 1, for instance, shifted close to the 600 MHz lower bound cutoff and, as a result, the markers for  $f_1$  and  $f_a$  were not visible. This tag could, therefore, not be used for  $\mu_{eff}$  estimation.

Confirming our reasoning above would require electromagnetic simulations with TUTs, which is beyond the scope of this paper. However, these findings do indicate that the hypothesis is not universally applicable to all T-matched tags, and that every tag of interest (with specific antenna and specific IC) needs to be explicitly evaluated for the MUTs. Nevertheless, as one can see from Table V, it works well for many T-matched tags on moderate dielectrics.

# VII. CONCLUSION AND FUTURE WORK

In this paper we demonstrated how AT code changes could be used as markers to estimate the POTF resonance frequencies  $(f_a \text{ and } f_b)$  and dipole resonance frequency  $(f_1)$  of antennas with a T-match structure. We also demonstrated how the POTR resonance frequency

 $(f_c)$  and loop resonance  $(f_2)$  could be derived from these markers.

Our approach simply requires reading the AT code across the frequency band and does not need to precisely measure reader output power or received tag RSSI, nor have knowledge of the environment or read distance. It can be viewed as a form of near-field sensing since AT code is not affected by the far field channel characteristics and is affected only by interaction of the tag antenna with a dielectric or magnetic object in its near field.

We showed how  $f_c$  values derived from our method could be used to reliably estimate effective dielectric permittivity ( $\epsilon_{eff}$ ) of the material to which the tag is attached using 6 different tags with different antenna designs and attached chips. We also showed that our approach worked well in both real and idealized testing scenarios. Additionally, we demonstrated how  $f_2$  values derived from AT markers could be used to estimate the effective magnetic permeability ( $\mu_{eff}$ ) for at least 2 tags placed on a FAM magneto-dielectric substrate in an idealized environment. The estimates from the two tags were in good agreement with one another.

There are several avenues of future work that are being considered. First, we have pointed out the reasoning for the limitations of our work and would like to verify those by electromagnetically simulating the performance of antennas that do not conform to our hypothesis. In the process, we would also like to estimate the true  $\mu_r$  and  $\epsilon_r$  of the FAM.

Second, we would also like to see if chips with additional capacitance states, such as Axzon's Magnus, could be used to generalize the hypothesis to more antenna geometries. Designing new tag antennas for those chips, which would have both POTF and POTR resonances on several dielectrics visible inside Voyantic 600-1300 MHz band, would be an interesting experiment for our hypothesis. We would also like to see if tags that have POTR peaks (in air) significantly higher than Tag 5 could be used to sense more magneto-dielectric materials, such as tags encased in 2 FAM sheets as presented in [8].

We would also like to investigate the dependence of chip impedance on input power. Specifically, if there are frequency regimes where the chip impedance is not significantly dependent on input power, and if those frequencies can be aligned with the tag antenna's resonance frequencies, then one does not need to take measurements at threshold power levels. Threshold power determination is time consuming and therefore taking measurements at arbitrary transmit power settings would speed up the sensing measurements. This would also allow to use a simple low-cost wideband software defined radio (SDR) RFID reader with fixed output power to do AT code measurements described in this paper.

In addition, our approach still requires sweeping the 600-1300 MHz band, which necessitates the use of broadband reader equipment. To enable the use of commercial RFID readers for sensor readings, we aim to examine arrays of tags, each having AT code markers that fall within the ISM band when attached to different MUTs.

Finally, we would also like to expand the testing to additional materials with higher  $\epsilon_r$  and loss tangent  $tan(\delta)$ .

#### REFERENCES

- (Simply RFID, Warrenton, VA, USA). SimplyRFiD Adds Support for 128-Bit RAIN RFID Tags. Accessed: Jan. 16, 2025. [Online]. Available: https://www.simplyrfid.com/press/simplyrfid-adds-support-for-128-bit-rain-rfid-tags/
- [2] N. Eaton. "Walmart expands RFID mandate: What it means for RAIN RFID in retail." Impinj Insights. Accessed: Jan. 16, 2025. [Online]. Available: https://www.impinj.com/library/blog/walmart-makes-big-rfid-commitment-with-sweeping-tag-mandate
- [3] J. P. Harrison et al., "Biodegradability standards for carrier bags and plastic films in aquatic environments: A critical review," *Royal Soc. Open Sci.*, vol. 5, May 2018, Art. no. 171792.
- [4] N. A. Mohammed, K. R. Demarest, and D. D. Deavours, "Analysis and synthesis of UHF RFID antennas using the embedded T-match," in *Proc. IEEE Int. Conf. RFID (IEEE RFID)*, 2010, pp. 230–236.
- [5] "Voyantic TagFormance pro." Accessed: Jan. 16, 2025. [Online]. Available: https://voyantic.com/lab/tagformance-pro/
- [6] P. Nikitin, J. Kim, and K. Rao, "RFID tag analysis using an equivalent circuit," in *Proc. IEEE Int. Symp. APS/URSI*, 2021, pp. 167–168.
- [7] P. Nikitin, M. Brewster, J. Kim, and K. Rao, "Dielectric sensing using T-matched RAIN RFID tags," in *Proc. IEEE Int. Conf. RFID*, 2023, pp. 42–47.
- [8] P. Nikitin, M. Brewster, J. Kim, and K. Rao, "Magnetic sensing using T-matched RAIN RFID tags," in *Proc. IEEE Int. Conf. RFID*, 2024, pp. 1–6.
- [9] M. Cotton. "Read AutoTune value in Voyantic Tagformance threshold measurements," Impinj. Accessed: Apr. 2, 2025. [Online]. Available: https://support.impinj.com/hc/en-us/articles/360016583919-Read-AutoTune-Value-in-Voyantic-Tagformance-Threshold-Measurements
- [10] "UCODE 9 accelerates the IoT." NXP. Accessed: Mar. 28, 2025.
  [Online]. Available: https://www.nxp.com/products/SL3S1206FUD2
- [11] "Magnus-3." AXZON. Accessed: Mar. 28, 2025. [Online]. Available: https://www.axzon.com
- [12] "AS3213C—External sensor with capacitive analog interface." Asygn. Accessed: Apr. 12, 2025. [Online]. Available: https://asygn.com/as3213c-external-capacitive/
- [13] M. C. Caccami and G. Marrocco, "Electromagnetic characterisation of self-tuning UHF RFID tags for sensing application," in *Proc. IEEE AP-S/URSI*, 2016, pp. 1273–1274.
- [14] F. Piccinno, F. Naccarata, R. Colella, F. P. Chietera, L. Catarinucci, and G. Marrocco, "Exploiting self-tunable RFID chips for wireless sensing of permittivity to enable passive low-cost food-quality monitoring systems," in *Proc. IEEE 13th RFID-TA*, 2023, pp. 45–48.
- [15] G. M. Bianco and G. Marrocco, "Joint design of self-tuning UHF RFID antenna and microfluidic channel for liquid sensing," *IEEE J. Radio Freq. Identif.*, vol. 8, pp. 58–67, 2024.
- [16] F. Naccarata, G. M. Bianco, and G. Marrocco, "Sensing performance of multi-channel RFID-based finger augmentation devices for tactile Internet," *IEEE J. Radio Freq. Identif.*, vol. 6, pp. 209–217, 2022.
- [17] D. Dutta, S. Genovesi, G. Manara, and F. Costa, "Characterization of material resistivity by using a self-tunable chip for gas sensing application," in *Proc. IEEE AP-S/INC-USNC-URSI*, 2024, pp. 1611–1612.
- [18] D. Dutta, S. Genovesi, G. Manara, and F. Costa, "Characterization of material properties by using an auto-tuned RFID chip," in *Proc. 4th* URSI AT-RASC, 2024, pp. 1–4.
- [19] F. Nanni, S. Nappi, and G. Marrocco, "Potentiometric sensing by means of self-tuning RFID ICs," in *Proc. IEEE Int. Conf. RFID (RFID)*, 2022, pp. 17–22.
- [20] A. Shastri, I. Ullah, and B. Sanz-Izquierdo, "Alternating current sensing slot antenna," *IEEE Sensors J.*, vol. 21, no. 7, pp. 9484–9491, Apr. 2021.
- [21] A. Mostaccio, C. Miozzi, S. Amendola, C. Occhiuzzi, and G. Marrocco, "Experimental characterization of zero-power RFID-based strain sensor for implanted Fixators," in *Proc. IEEE MetroInd4.0 IoT*, 2024, pp. 506–511.
- [22] L. Rauter et al., "Printed single-chip RFID tags on uncoated paper for environmental monitoring applications," *IEEE Sens. Lett.*, vol. 9, no. 5, pp. 1–4, May 2025.
- [23] K. Zannas, H. El Matbouly, Y. Duroc, and S. Tedjini, "Self-tuning RFID tag: A new approach for temperature sensing," *IEEE Trans. Microw. Theory Techn.*, vol. 66, no. 12, pp. 5885–5893, Dec. 2018.
- [24] (Avery Dennison, Mentor, OH, USA). First Passive UHF Moisture-Sensing Inlay on the Market. Accessed: Mar. 28, 2025. [Online]. Available: https://rfid.averydennison.com/en/home/news-insights/ insights/automotive-first-passive-uhf-moisture-sensing-inlay-on-themarket.html

- [25] P. Nikitin, J. Kim, G. Berzagui, J. M. Roehe, and K. Rao, "Reversed T-matching in RFID tag antennas," in *Proc. IEEE AP-S/URSI*, 2022, pp. 119–120.
- [26] M. Lenehan. "Impinj M700 series tag chips product brief." Impinj. Accessed: Apr. 5, 2025. [Online]. Available: https://support.impinj. com/hc/en-us/articles/360010797539-Impinj-M700-Series-Tag-Chips-Product-Brief-Datasheet
- [27] "RAIN RFID tags from Impinj partners." Impinj. Accessed: Jan. 21, 2025. [Online]. Available: https://www.impinj.com/partners/products/ partner-tags?pagesize=500
- [28] "Reference material set." Voyantic. Accessed: Jan. 17, 2025. [Online]. Available: https://voyantic.com/lab/tagformance-pro/accessories/
- [29] "Sheet suppressors." Delevan. Accessed: Apr. 7, 2025. [Online]. Available: https://www.delevan.com/en/products/suppressors
- [30] A. Abbosh, "Accurate effective permittivity calculation of printed Center-fed dipoles and its application to quasi Yagi-Uda antennas," *IEEE Trans. Antennas Propag.*, vol. 61, no. 4, pp. 2297–2300, Apr. 2013. [Online]. Available: https://doi.org/10.1109/tap.2012.2231925
- [31] (Avery Dennison, Mentor, OH, USA). AD Dogbone R6. Accessed: Apr. 12, 2025. [Online]. Available: https://rfid.averydennison.com/content/dam/rfid/en/products/rfid-products/data-sheets/datasheet-Dogbone-Monza-R6.pdf
- [32] "AZ-HR7A." Arizon. Accessed: Apr. 12, 2025. [Online]. Available: https://www.arizonrfid.com/product-AZ-HR7A-AZ-HR7A.html



Fatima Villa Gonzalez (Member, IEEE) received the bachelor's degree in telecommunications systems engineering and the M.Sc. degree in telecommunications engineering from Tecnun in 2017 and 2019, respectively, and the Ph.D. degree in electrical and electronics engineering from Tecnun, University of Navarra, Spain, in 2023. She joined the Auto-ID Labs, Massachusetts Institute of Technology, in 2019 to conduct her M.Sc. Thesis. She has been closely working with them since then, where she is currently a Postdoctoral Associate. She is interested in applied

research related to wireless sensors, especially chipped and chipless RFID sensor design and development, and signal processing. She was the recipient of the 2024 IEEE RFID-TA Conference Women Best Paper Award.



Rahul Bhattacharyya (Senior Member, IEEE) received the Ph.D. degree in systems engineering from the Massachusetts Institute of Technology (MIT), Cambridge, MA, USA, in 2012, where he is currently the Director with the Auto-ID Labs. He has authored over 50 technical peer reviewed publications. His research encompasses the development and integration of technologies that form the framework for the Internet of Things (IoT). He was the recipient of the 2020 IEEE Sensors and 2015 IEEE RFID-TA Conference Best Paper Award. He

has also been awarded two U.S. and two international patents for his work. He is an Associate Editor for IEEE SENSORS JOURNAL. He has also served as the TPC Chair of IEEE RFID from 2018 to 2019 and the 4th International Conference on the IoT 2014 at MIT.



Pavel Nikitin (Fellow, IEEE) received the Ph.D. degree in electrical and computer engineering from Carnegie Mellon University in 2002. He is currently a Technical Fellow with Impinj Inc., Seattle, WA, USA, where he is doing research, design, and development of RAIN RFID tags and systems products. He previously worked with Honeywell, Intermec, IBM, and Ansys. He is also an Affiliate Associate Professor with the Electrical and Computer Engineering Department, University of Washington. He received four best paper awards,

has over 50 U.S. patents, and over 60 IEEE publications.